

# The diameter factor of aligned membranes facilitates wound healing by promoting epithelialization in an immune way

Chenbing Wang<sup>a,1</sup>, Chenyu Chu<sup>a,1</sup>, Xiwen Zhao<sup>a,1</sup>, Yang Yang<sup>a</sup>, Chen Hu<sup>a</sup>, Li Liu<sup>c</sup>, Jidong Li<sup>b</sup>, Yili Qu<sup>a</sup>, Yi Man<sup>a,\*</sup>

<sup>a</sup> Department of Oral Implantology & National Clinical Research Center for Oral Diseases & State Key Laboratory of Oral Diseases, West China Hospital of Stomatology, Sichuan University, Chengdu, China

<sup>b</sup> Research Center for Nano-Biomaterials, Analytical and Testing Center, Sichuan University, Chengdu 610064, China

<sup>c</sup> State Key Laboratory of Biotherapy, West China Hospital, Sichuan University, Collaborative Innovation Center for Biotherapy, Chengdu, Sichuan 610041, China

## ARTICLE INFO

### Keywords:

Aligned membranes  
Diameter  
Wound healing  
Epithelialization  
MMP12

## ABSTRACT

Topographical properties, such as pattern and diameter, of biomaterials play important roles in influencing cell activities and manipulating the related immune response during wound healing. We prepared aligned electrospinning membranes with different fiber diameters, including  $319 \pm 100$  nm (A300),  $588 \pm 132$  nm (A600), and  $1048 \pm 130$  nm (A1000), by adjusting the distance from the tip to the collector, the injection rate, and the concentration of the solution. The A300 membranes significantly improved cell proliferation and spreading and facilitated wound healing (epithelization and vascularization) with the regeneration of immature hair follicles compared to the other membranes. Transcriptomics revealed the underlying molecular mechanism that A300 could promote immune-related processes towards a pro-healing direction, significantly promoting keratinocyte migration and skin wound healing. All the results indicated that wound healing requires the active participation of the immune process, and that A300 was a potential candidate for guided skin regeneration applications.

## 1. Introduction

Skin, a superficial organ in contact with the surrounding environment, constitutes the first important guard against external hazards [1]. The inability to re-epithelialize wounded skin can contribute to de-watening, inflammation, and even mortality [2,3]. Therefore, it is very important to close the wound quickly to restore the skin barrier that is essential for the survival of the organism. Regrettably, current strategies for managing large wounds are not satisfactory since they are dependent on both slow and passive healing processes [4]. Promoting skin healing with the regeneration of skin appendages, such as hair follicles (HFs), that are closely related to skin tensile strength and are an important index of skin functional healing [5] has not been truly realized [6]. Consequently, there is a growing need for exploring advanced grafts to achieve ideal re-epithelialization with appendages [7–9].

The electrospinning membrane is an ideal alternative for wound healing [10,11] because it imitates the topography and functions of the

extracellular matrix (ECM) [12,13], provides a moist environment, allows gas exchange, avoids bacterial infiltration [14], and manipulates immune-related processes towards a pro-healing direction [15,16]. Aligned membranes have a wide range of applications in the field of wound healing [1,17,18] since they can provide a series of biochemical and physical cues for regulating cell behaviors and influencing the immune response [19]. For example, it has been reported that fibroblasts can migrate over a long distance in a highly correlated manner and at a constant speed on aligned membranes [20,21]. Aligned membranes could promote the normal differentiation and outgrowth of vascular smooth muscle cells [17,22]. Critically, previous research in our group has shown that aligned membranes have many advantages in soft tissue repair and can actively regulate the immune response [23].

Although already widely used as skin wound healing biomaterials, the inflammation resistance and mechanical properties of aligned membranes still need to be strengthened [24] before broader applications are possible. Many studies have attempted to improve the

Peer review under responsibility of KeAi Communications Co., Ltd.

\* Corresponding author. Department of Oral Implantology, State Key Laboratory of Oral Diseases, West China Hospital of Stomatology, Sichuan University, 14#, 3rd section, Renmin South Road, Chengdu 610041, China.

E-mail address: [manyi780203@126.com](mailto:manyi780203@126.com) (Y. Man).

<sup>1</sup> These authors contributed equally to this work.

<https://doi.org/10.1016/j.bioactmat.2021.09.022>

Received 26 June 2021; Received in revised form 1 September 2021; Accepted 16 September 2021

Available online 24 September 2021

2452-199X/© 2021 The Authors. Publishing services by Elsevier B.V. on behalf of KeAi Communications Co. Ltd. This is an open access article under the CC

BY-NC-ND license (<http://creativecommons.org/licenses/by-nc-nd/4.0/>).

mechanical properties and biological performance of aligned membranes by adjusting their microstructure, since topographical factors could affect early cell fate prior to cytokines [25,26]. In view of the fact that the ECM is composed of fibers of different sizes, from nano-to-micron-scale, the diameter factor that dictates the physicochemical properties and biological performances of membranes was introduced [27]. For example, human skin fibroblasts have a well-diffused

morphology, growing on membranes with 350–1100 nm fiber diameters, and the expression of the type-III collagen gene in human skin fibroblasts was significantly upregulated [28]. It was found that there was a critical minimum membrane fiber diameter ( $d$ ), namely 0.97  $\mu\text{m}$ , that made the human fibroblasts develop better directionally, in contrast to membranes with  $d < 0.97 \mu\text{m}$  [29]. Additionally, membranes with small diameter fibers (about 250–300 nm) were a stronger support for

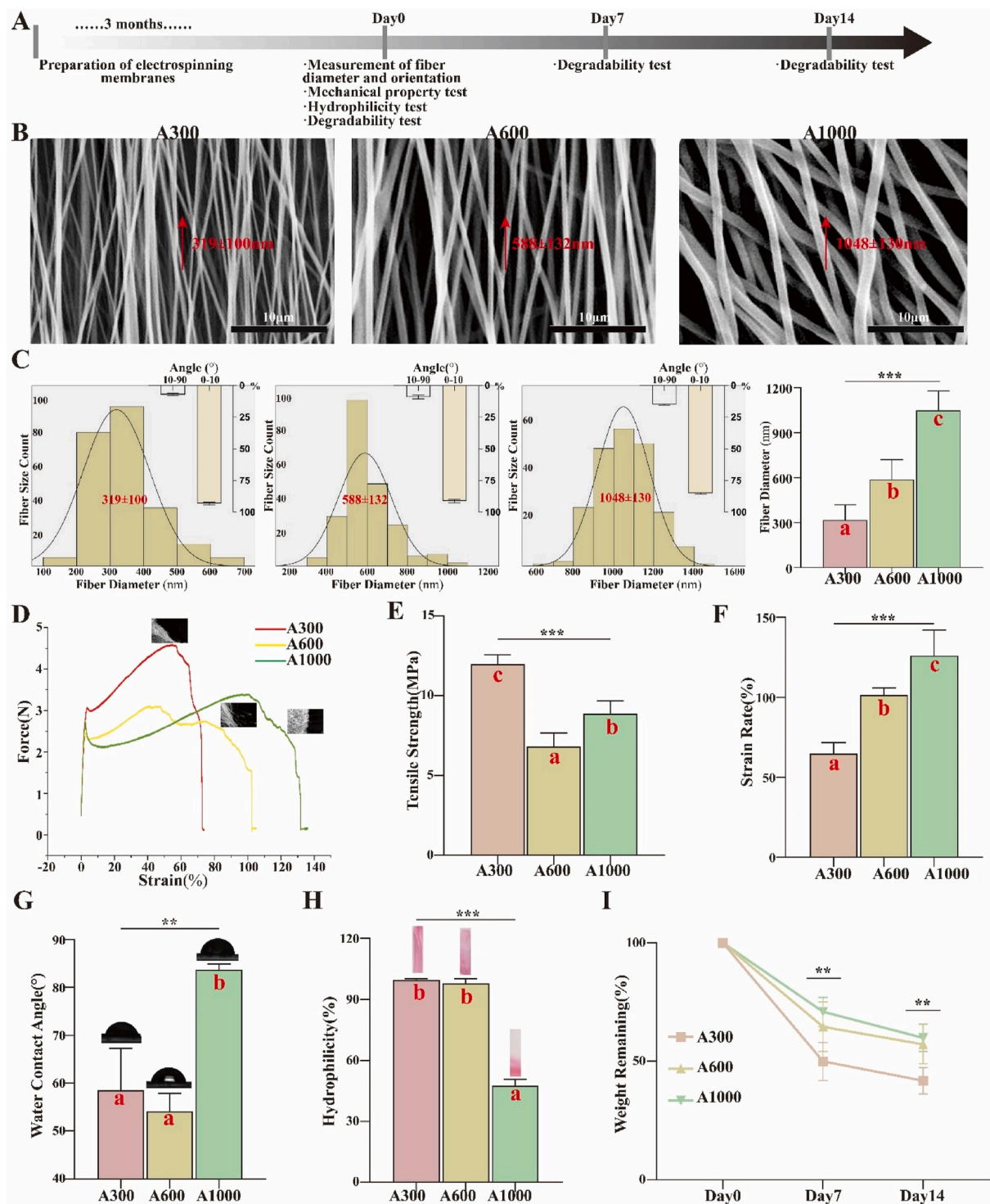


**Fig. 1.** (A) Workflow for evaluating physicochemical properties of electrospinning membranes; (B) SEM images and (C) corresponding diameter distributions of different diameter aligned membranes; (D) Typical stress–strain curves of various membranes (parallel to aligned membranes); (E) Tensile strength; (F) Strain rate; (G) WCA images and corresponding analysis; (H) Hydrophilicity images and corresponding analysis; (I) Degradation assays. \* $p < 0.05$ , \*\* $p < 0.01$ , \*\*\* $p < 0.001$  by ANOVA for data in (C), (E), (F), (G), (H), and (I). Different letters indicate significant differences.

dermal fibroblast proliferation than membranes composed of fibers with a diameter of about 1  $\mu\text{m}$  [30]. It has been reported that biological nanofiber membranes could also induce and enhance stem cell differentiation compared to microfibers and play an important role in promoting regeneration [31–33]. Another study has revealed that the fiber diameter of membranes could affect the immune response of macrophages, especially in the early stage of inflammation, since nanofiber membranes minimize the inflammatory response relative to microfiber membranes [34] and manipulate tissue regenerative immune reactions [35].

Studies involving fibroblasts and monocytes/macrophages have corroborated the positive effect of the diameter factor of aligned membranes on cell behavior. However, the results of the abovementioned studies are controversial. The specific characteristics of these aligned membranes, especially which diameter interval is most suitable for tissue regeneration, need to be verified. In addition, the potential diameter-mediated mechanism of repairing tissue defects has not been explored. Here, we explore the skin defect response to aligned biosynthetic membranes with varying fiber diameters, including  $319 \pm 100$  nm (A300),  $588 \pm 132$  nm (A600), and  $1048 \pm 130$  nm (A1000) [36,37], to develop a more suitable surface wound healing medical device for manipulating the related immune response and promoting re-epithelialization with appendages. In this comprehensive study, we also evaluate the transcriptome of rat skin wounds on the aligned membranes of varying fiber diameters to explore the potential diameter-mediated mechanism of repairing tissue defects.

## 2. Results

### 2.1. A300 improves the mechanical stability, hydrophilicity, and degradation of aligned membranes

**Topological and mechanical properties.** The workflow for evaluating physicochemical properties of aligned membranes with different diameters is summarized in Fig. 1A. The topology and corresponding fiber diameter distributions of membranes are shown as  $319 \pm 100$  nm (A300),  $588 \pm 132$  nm (A600), and  $1048 \pm 130$  nm (A1000) in Fig. 1B and C. Fiber diameter differences were statistically significant ( $p < 0.05$ ), revealing that the fibers presented a homogeneously bead-less performance and a highly aligned morphology. The electrospinning parameters are shown in Table S1. The preliminary experiments are shown in Fig. S1. Based on the histogram in Fig. 1C, the mean diameter of the aligned fibers was reduced with the change of the distance from the tip to the collector, the injection rate, and solution parameters. The membrane was ultimately formed, collected at the roller collector (2800 rpm), and covered with a piece of aluminum foil. This is mainly because the increase in the electric field promoted the stretch rate of electrospinning fibers and the decrease of poly (lactic-co-glycolic-acid) (PLGA) restrained the electrospinnability itself, resulting in electrospinning fibers with a narrower size distribution and smaller mean diameter [30]. It is typically assumed that submicron-scale bioscaffolds possess better pro-healing effects for tissue engineering, since the main advantage of submicron-scale features over micron-scale features is that they provide a larger surface area to adsorb proteins and form more adhesion sites to integrin [38,39]. The mechanical performance of aligned membranes is an important determinant for their application in wound healing, because they are expected to present suitable mechanical strength during surgery and tissue regeneration.

In this experiment, we evaluated the mechanical behaviors of different aligned membranes (before crosslinking) via tensile strength tests. The stress–strain curve (Fig. 1D and E) illustrates that the tensile strength of small diameter aligned membranes (A300,  $11.95 \pm 0.35$  MPa) was elevated compared with medium diameter (A600,  $6.80 \pm 0.49$  MPa) and large diameter (A1000,  $8.86 \pm 0.47$  MPa) membranes ( $p < 0.05$ ). Meanwhile, the strain rate of A300 ( $64.73 \pm 3.51\%$ ) is maintained a lower level (Fig. 1F) compared to A600 ( $101.3 \pm 2.37\%$ ) and

A1000 ( $126.2 \pm 8.01\%$ ) ( $p < 0.05$ ). The smaller diameter apparently increases the mechanical stability of aligned membranes, which could prevent scars in skin wound healing [40]. The mechanical performance of these membranes could be partially explained by the fracture process of fibers. This is primarily because membranes comprised of smaller diameter fibers have both higher strength and lower ductility [41,42].

**Roughness and physicochemical properties.** As shown in Figs. S2A–C, the roughness of aligned membranes seems to improve with the increase of mean diameter, consistent with the abovementioned results from scanning electron microscope (SEM) studies, and are beneficial for cell adhesion and migration to some extent [43]. Nevertheless, the differences between membrane diameter groups are not statistically significant. The aligned membranes possess a high specific surface area, which provides a larger surface area for cell adhesion [11], prevents undesirable fluid accumulation, and accommodates more facile oxygen permeation [44]. In this study, the alignment of A300 is similar to that of A600 and much better than that of A1000, indicating a potential for vascularization when using smaller diameter membranes [17] (Fig. S2D).

**Hydrophilicity and *in vitro* degradation behavior.** The hydrophilicity of the aligned membranes was investigated by water contact angle (WCA) assay. As shown in Fig. 1G, the A300 aligned membranes exhibit a WCA of  $58.52 \pm 5.06^\circ$ , similar to that of A600 ( $54.15 \pm 2.14^\circ$ ) and less than that of A1000 ( $83.69 \pm 0.67^\circ$ ) ( $p < 0.05$ ), which demonstrates its hydrophilic behavior of aligned membranes. It has been shown that decreasing fiber diameter significantly increases the water affinity of aligned membranes. This is mainly because the high specific surface area conveniently interacts with water molecules. The morphology of a biomaterial directly dictates its hydrophilicity, ultimately determining the WCA. Apart from fiber diameter, fiber arrangement and surface roughness exert significant influence on the hydrophilicity of aligned membranes [45]. We further studied the hydrophilic behavior by evaluating the infiltration of these three groups of aligned membranes. As shown in Fig. 1H, the A300 aligned membrane is completely wetted, marginally more than A600 ( $97.86 \pm 1.32\%$ ) and significantly more than A1000 ( $47.54 \pm 1.81\%$ ) ( $p < 0.05$ ), consistent with the aforementioned result in the WCA assay.

Ideal implanted biomaterials, such as wound dressings, should have suitable mechanical strength as well as matched biodegradability. Fiber degradation gradually destroys the structural and functional integrity of aligned membranes and provides the space and nutrients for new tissue ingrowth. In order to evaluate the degradability of the membranes *in vitro*, we monitored the remaining mass during the immersion process. As shown in Fig. 1I, the mass remaining from A300 membranes is significantly smaller than those of the others both on day 7 (A300:  $50.02 \pm 3.58\%$ , A600:  $64.65 \pm 4.64\%$ , and A1000:  $70.97 \pm 2.73\%$ ) and on day 14 (A300:  $41.84 \pm 2.47\%$ , A600:  $57.24 \pm 3.71\%$ , and A1000:  $59.99 \pm 2.58\%$ ) ( $p < 0.05$ ). The results show that decreasing fiber diameter accelerates the degradation process of fibers, hence advancing the degradation of aligned membranes (the degradation of membranes *in vivo* is shown in Fig. S3A).

### 2.2. A300 promotes fibroblast proliferation and accelerates keratinocyte spreading on the aligned membranes

The workflow for evaluating the cell-membrane interaction of aligned membranes is summarized in Fig. 2A. Before clinical application as wound dressings, the different diameter aligned membranes should be assessed for performance in the ability to ameliorate related cell proliferation and/or migration. Accordingly, the proliferation of fibroblasts (L929) and human oral keratinocytes (HOK) on different diameter aligned membranes was assessed, as shown in Fig. 2B and C. For L929, the proliferation rate on A300 membranes is significantly higher than on the other membranes, except for the control group. However, there is no statistically significant difference in HOK proliferation between the membrane groups. The results indicate that the A300 membrane is more



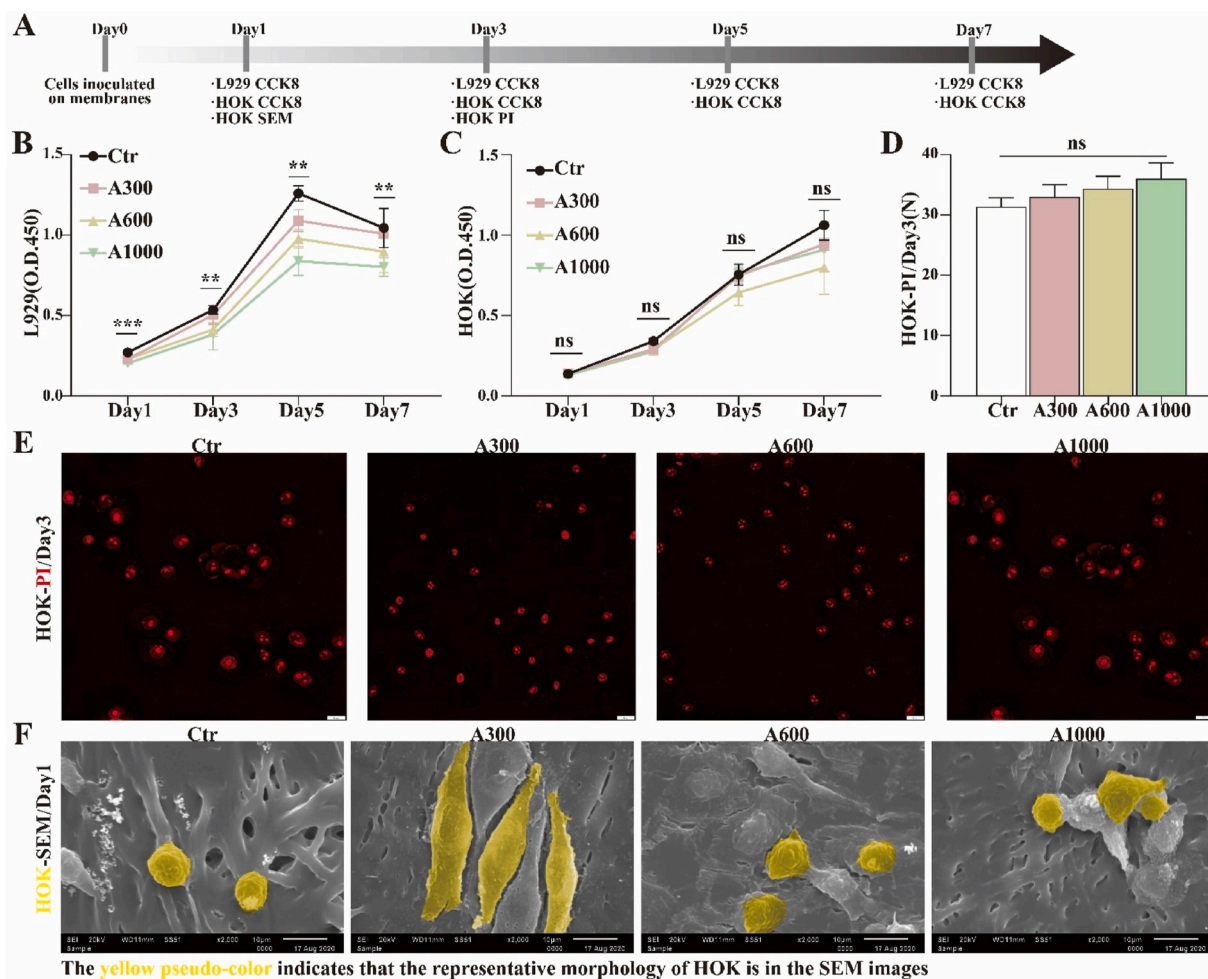


**Fig. 2.** (A) Workflow for evaluating the biocompatibility of electrospinning membranes; CCK-8 tests of (B) L929 and (C) HOK; (D) Analysis and (E) corresponding images of PI fluorescent staining of HOK; (F) SEM images of HOK morphology. \* $p < 0.05$ , \*\* $p < 0.01$ , \*\*\* $p < 0.001$  by ANOVA for data in (B), (C), and (D).

conductive for the proliferation of L929, but fiber diameter seems to have no significant influence on the proliferation of HOK [46]. It has been reported that cell proliferation on membranes is intimately related to fiber diameter and topological structure, which directly affect cell adhesion and the exchange of nutrients [28,30,34]. The fiber diameter of the aligned membranes decreased from  $1048 \pm 130$  nm to  $319 \pm 100$  nm with the change of operation and solution parameters, promoting cell adhesion and proliferation of cells on A300 [47].

**Viability and morphology.** In order to clarify the effect of different aligned membrane diameters on HOK, we further studied the viability and morphology of HOK using fluorescent staining with propidium iodide (PI) and SEM. As shown in Fig. 2D and E, dead HOK on A300 aligned membranes ( $33.0 \pm 1.2$ ) is marginally less than on A600 ( $34.3 \pm 1.2$ ) and A1000 ( $36.0 \pm 1.5$ ) on day 3, with no statistically significant difference. Additionally, as presented in Fig. 2F, SEM reveals that HOK spread on the A300 aligned membranes is much better than on A600 and A1000 on day 1. This is consistent with previous studies that showed that cells adhered to nanofibers proliferated much better than those adhered to microfibers [48]. Overall, membrane fiber diameter may have different degrees of positive effects on different types of cells, such as promoting L929 proliferation and accelerating HOK spread. Our results also indicate that the surface properties of aligned membranes, including diameter, wettability, and roughness, seem to affect the biological behavior of L929 and HOK. Additionally, the biosafety of the membranes *in vivo* is shown in Fig. S3B. Expression of actin, fibronectin (FN), and collagen IV (Col IV) in fibroblasts is elevated in A300 compared to other groups, as shown in Fig. S4 [49,50].

### 2.3. A300 significantly facilitates wound healing

**General Situation.** The workflow for evaluating rat skin wound healing is summarized in Fig. 3A. In practical application, the membranes utilized for wound dressings could accelerate related wound healing. Accordingly, the restoration performance of aligned membranes with different diameters was assessed on rat skin defects, as shown in Fig. 3B and C. For rat skin defects, the residual area of the A300 group is significantly smaller than those of the others at all time points. Intriguingly, the wounds treated with A300 membranes occasionally reached complete healing one or two days earlier. The macroscopic result indicates that the small fiber diameter membranes were indeed better for the reconstruction of rat skin defects, consistent with the *in vitro* results. We further studied wound healing by evaluating the hematoxylin and eosin (H&E) staining of tissue sections. As shown in Fig. 3D and E, the residual gap of the A300 group ( $2.70 \pm 0.18$  mm) is significantly narrower than that of the A600 ( $3.63 \pm 0.06$  mm) and the A1000 ( $4.15 \pm 0.05$  mm) groups on day 7 ( $p < 0.05$ ), confirming the previous macroscopic result that rat skin defects close faster when treated with A300 aligned membranes.

**Foreign body response.** The performance of aligned membranes is built on the compatible interaction between the membrane and the host immune defense system [51], since the immune recognition system initiates the foreign body response (FBR). The FBR comprises continuous inflammation, fibrosis (formation of a fibrous capsule), and damage to the surrounding tissue [52,53]. These unwanted outcomes may destroy the function of aligned membranes and lead to pain and discomfort at

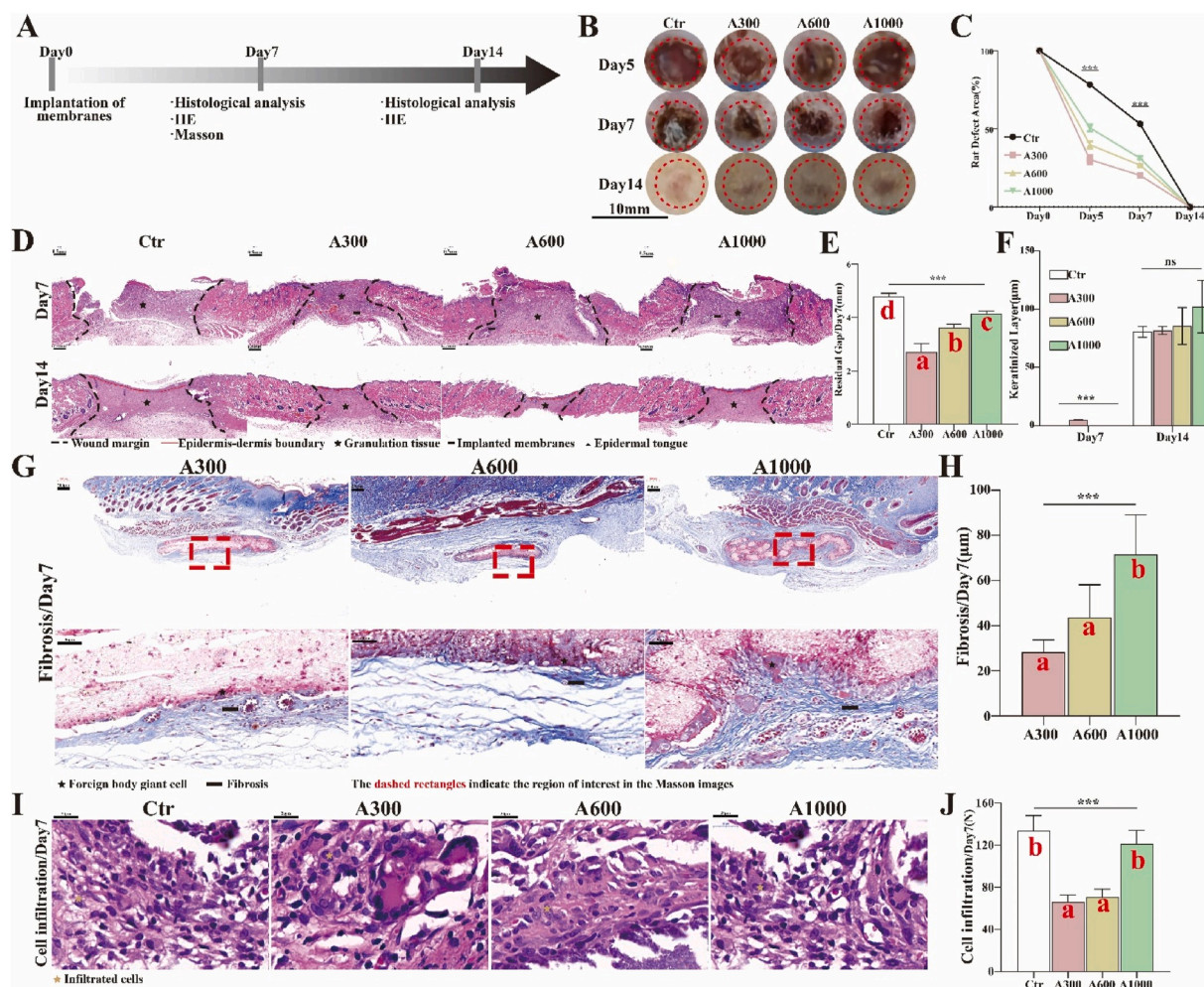


**Fig. 3.** (A) Workflow for evaluating rat skin wound healing and FBR; (B) Macroscopic images of rat skin defects and (C) corresponding analysis; (D) Residual gap images of H & E of rat skin defects and (E) corresponding analysis; (F) The analysis of keratinized layer images of H & E; (G) FBR images of MST Staining of rat subcutaneous implantations and (H) corresponding analysis; (I) Cell infiltration images of H & E of rat skin defects and (J) corresponding analysis. \* $p < 0.05$ , \*\* $p < 0.01$ , \*\*\* $p < 0.001$  by ANOVA for data in (C), (E), (F), (H), and (J). Different letters indicate significant differences.

the recipient site [54]. In this study, the macroscopic result of rat skin defects shows that, on day 14, better wound healing occurs and less scar tissue forms with the use of A300 membranes (Fig. 3B). We further investigated the thickness of fibrous capsules of rat subcutaneous implantations via Masson's trichrome staining (MST Staining) to evaluate the degree of FBR. As depicted in Fig. 3G and H, the thickness of the fibrous capsules of the A300-treated group ( $28.40 \pm 2.38 \mu\text{m}$ ) are significantly thinner than those associated with A600 ( $43.68 \pm 6.47 \mu\text{m}$ ) and A1000 ( $71.66 \pm 7.83 \mu\text{m}$ ) membranes, with statistically significant differences ( $p < 0.05$ ). There is minimum  $\alpha$  smooth muscle actin ( $\alpha$ SMA) expression *in vivo*, as shown in Fig. S5. Additionally, the number of cell infiltration recruited by A300 aligned membranes ( $66.00 \pm 3.79$ ) and A600 aligned membranes ( $70.67 \pm 4.33$ ) is less than that recruited by A1000 aligned membranes ( $121.0 \pm 7.37$ ) ( $p < 0.05$ ) (Fig. 3I and J). These studies together suggest that A300 aligned membranes could be compatible with the host immune defense system and indirectly give rise to the FBR for normal healing. Other studies have shown that nanofiber scaffolds minimize the inflammatory response relative to microfiber scaffolds [34].

**Vascularization.** The workflow for evaluating vascularization and epithelization is summarized in Fig. 4A. Based on the images in Fig. 4B and C, the results indicate that the degree of vascularization associated with A300 aligned membranes ( $0.250 \pm 0.009 \text{ mm}^2$ ) is significantly greater than that associated with A600 ( $0.125 \pm 0.002 \text{ mm}^2$ ) and with

A1000 ( $0.080 \pm 0.003 \text{ mm}^2$ ) aligned membranes on day 7 ( $p < 0.05$ ). This is further demonstrated by the dominant IHC staining (Fig. 4D and E) and corresponding RNA expression of CD31 in the A300 group (Fig. 4F).

**Epithelization.** Additionally, the keratinized layer of wounds appears first in A300-treated samples ( $4.78 \pm 0.08 \mu\text{m}$ ). The keratinized layer is not observed in wounds treated with the other aligned membranes even on the 7th day after operation. There is no significant difference between control and various diameter groups on day 14, whereas the thickness of the keratinized layer in A300 group is closer to that of the control group (Fig. 3F). This is further corroborated by immunofluorescence (IF) staining (Fig. 4G and H) and the corresponding RNA expression of cytokeratin 5/cytokeratin 10 (K5/K10) (Fig. 4I and J), both of which reveal that the degree of epithelization (continuity and differentiation) associated with A300 aligned membranes is significantly better than for the other groups. Also, the maximum number of newly formed (immature) hair follicles on day 14 (Fig. 4K) is associated with the A300 aligned membrane, demonstrating that the A300 aligned membranes achieve excellent repair results with regenerated appendages [55]. These studies show that the A300 aligned membranes increase both vascularization and epithelization, suggesting that A300 aligned membranes indeed accelerated rat wound healing. However, the specific mechanism of reducing inflammation/FBR and promoting skin wound healing remains unclear.



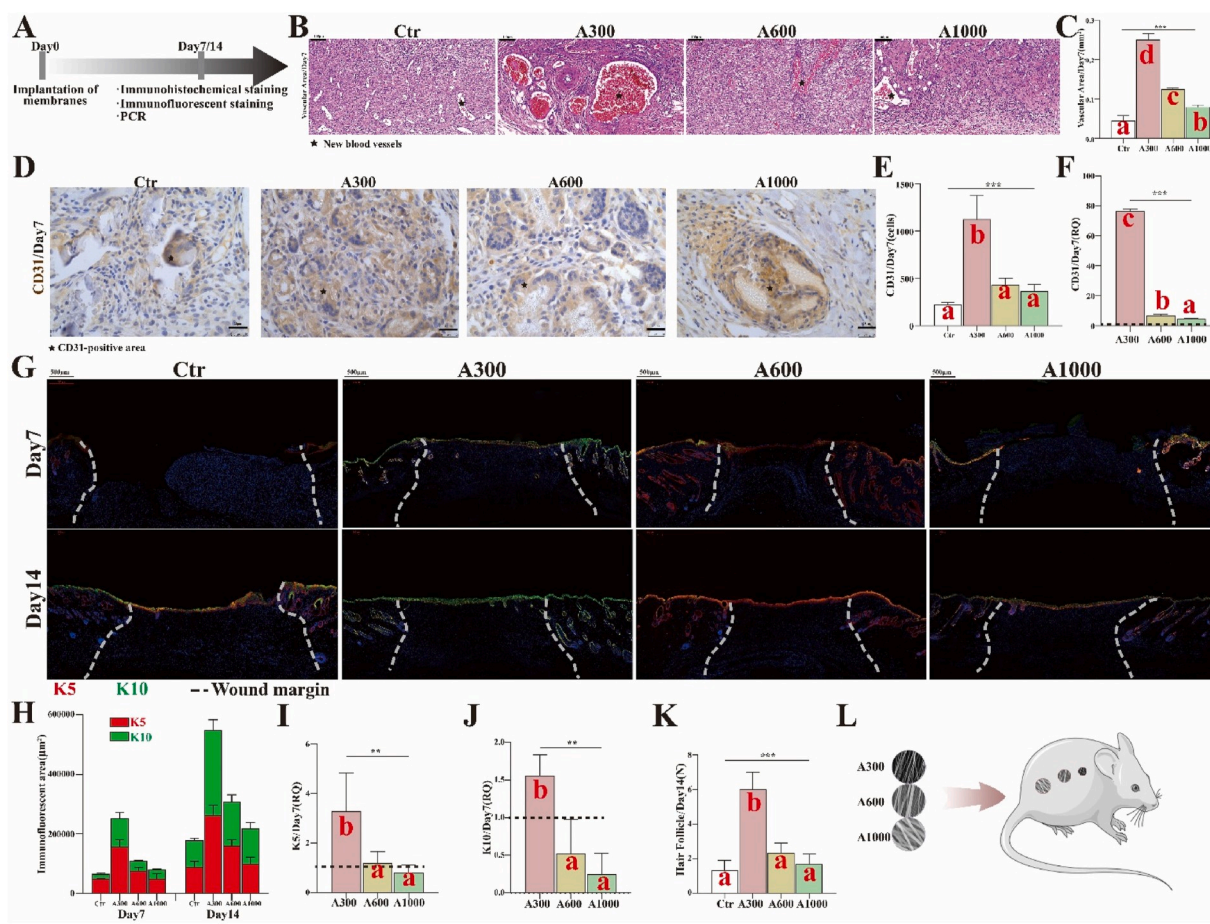


**Fig. 4.** (A) Workflow for evaluating vascularization and epithelization; (B) Vascularization images of H & E of rat skin defects and (C) corresponding analysis; (D) CD31-positive images of IHC staining of rat skin defects and (E) corresponding analysis; (F) RNA expression of CD31; (G) K5(red)/K10(green)-positive images of IF staining of rat skin defects and (H) corresponding analysis; (I) RNA expression of K5; (J) RNA expression of K10; (K) The number of regenerated HFs on day 14; (L) Different diameter aligned electrospinning membranes implanted on rat skin defects. \* $p < 0.05$ , \*\* $p < 0.01$ , \*\*\* $p < 0.001$  by ANOVA for data in (C), (E), (F), (I), (J), and (K). Different letters indicate significant differences.

#### 2.4. MMP12 is upregulated by A300 and promotes keratinocyte migration

In order to further explore the specific mechanism by which aligned membranes reduce inflammation/FBR for better wound healing, the bulk RNA sequencing of rat skin defects implanted with different diameter aligned membranes was studied via principal component analysis (PCA), Gene Ontology (GO), and Kyoto Encyclopedia of Genes and Genomes (KEGG) to screen the inflammation-related targets. The workflow for exploring the specific mechanism is summarized in Fig. 5A. The results of PCA show that A300 is different from other diameter groups and the control (Fig. 5B), suggesting that the diameter factor indeed plays a vital role in wound healing. As shown in Fig. 5C–E, the results of top 10 in GO show that the significantly upregulated biological process (BP) items associated with A300 include primarily immune-related processes, such as *positive regulation of immune response* and *innate immune response*, relative to control and A1000 groups. However, compared with A600, the significantly upregulated BP items associated with A300 are angiogenesis- and extracellular matrix-related processes, which probably account for the smaller difference in wound healing between A300 and A600.

The genes of immune-related processes that display significant changes have been presented as heat maps. From the heat maps (Fig. 5F and G), we learn that the expression associated with A300 is similar to that of A600 but much stronger than that of the control and A1000 in the abovementioned immune-related processes. This indicates that A300

could reduce inflammation/FBR, probably by actively regulating the immune response and achieving better wound healing. More importantly, the significantly differentially expressed matrix metalloproteinase 12 (MMP12) appears both in *positive regulation of immune response* and *innate immune response* of rat skin defects. Other studies have revealed that MMP12 actively regulates the migration of cells in the process of corneal wound healing [56,57]. We wondered whether MMP12 had a similar role in skin wound healing (Fig. 5H). For this reason, we evaluated the RNA and protein expression of MMP12 in rat skin defects implanted with different diameter aligned membranes through quantitative reverse transcription-polymerase chain reaction (qRT-PCR) and enzyme-linked immunosorbent assay (ELISA). The RNA and protein expression levels of MMP12 associated with A300 are higher than for other groups, and this difference is statistically significant (Fig. 5I and J). The *trans-well* experiments show that there are more migrating and more spreading HOK in the MMP12 group than in the MMP12 plus MMP408 (inhibitor of MMP12) and in the control group. This shows that the recombinant protein MMP12 promotes the migration and spread of HOK and that MMP408 inhibits the migration and spread effects of MMP12 (Fig. 5K–N) and indicates that MMP12 facilitates the migration and spread of epidermal cells. Screening for the optimal concentration of MMP12 for HOK migration is shown in Fig. 5G. Other growth factor/chemokine-induced migration experiments with no statistically significant difference, such as fibroblast migration towards PDGF (platelet-derived growth factor)-BB, keratinocyte migration induced by EGF (epidermal growth factor), and THP-1 cell migration

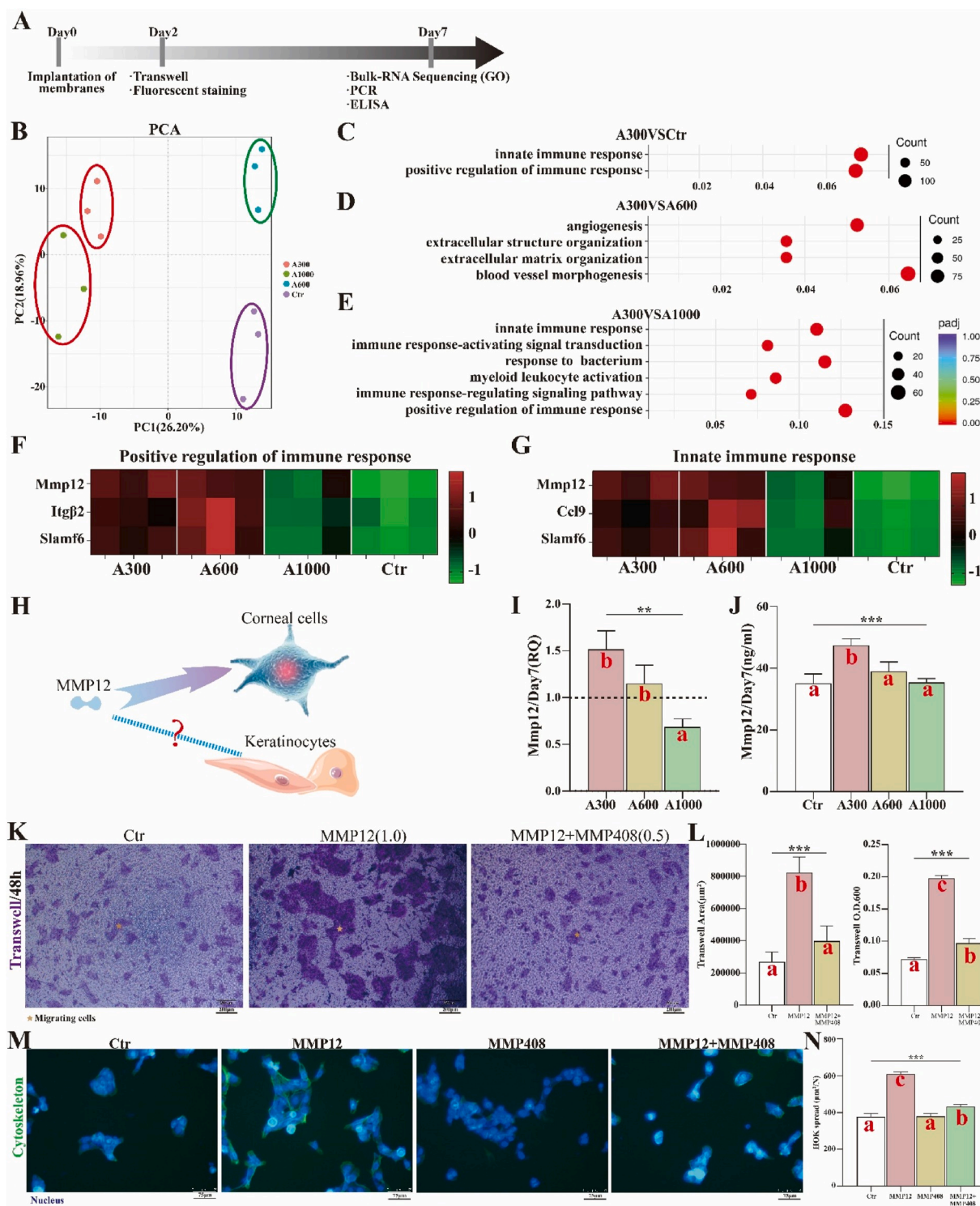


**Fig. 5.** (A) Workflow for exploring the function of MMP12 in rat skin defects; (B) PCA images of Bulk RNA sequencing on day 7; (C) A300VSCtr, (D) A300VSA600, and (E) A300VSA1000 of GO of Bulk RNA sequencing; (F) Heat map of *positive regulation of immune response*; (G) Heat map of *innate immune response*; (H) Proposed MMP12 function; (I) RNA expression of MMP12; (J) ELISA result of MMP12; (K) Trans-well assays on MMP12 promoting the migration of HOK and MMP408 inhibiting the function of MMP12 and (L) corresponding analysis; (M) Fluorescent staining of MMP12 promoting the spread of HOK and MMP408 inhibiting the function of MMP12 and (N) corresponding analysis. \* $p < 0.05$ , \*\* $p < 0.01$ , \*\*\* $p < 0.001$  by ANOVA for data in (I), (J), (L), and (N). Different letters indicate significant differences.

towards MCP (monocyte chemoattractant protein)-1, are shown in Fig. S7.

### 2.5. A300 promotes macrophage polarization to reparative phenotypes

The workflow for exploring the polarization of macrophages is summarized in Fig. 6A. MMP12 is commonly considered to be predominantly expressed by macrophages [58] (Fig. 6B). Phagocytosis, a



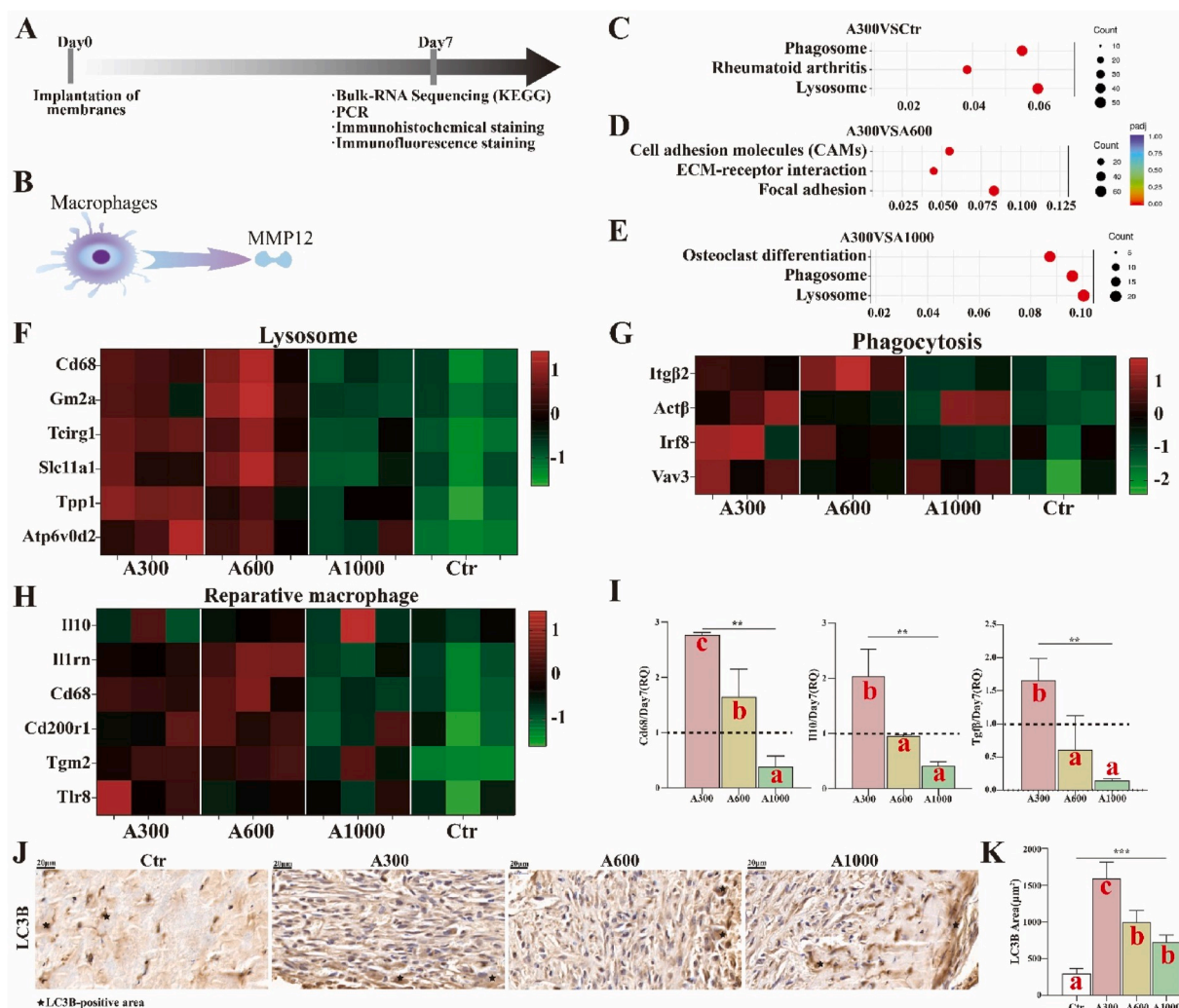


**Fig. 6.** (A) Workflow for exploring the transformation of macrophages; (B) The MMP12 secreted by macrophages; (C) A300VSCtr, (D) A300VSA600, and (E) A300VSA1000 of KEGG of Bulk RNA sequencing on day 7; (F) Heat map of lysosome; (G) Heat map of phagocytosis; (H) Heat map of reparative macrophages; (I) RNA expression of Cd68, IL10, and TGF $\beta$ ; (J) LC3B-positive images of IHC staining of rat skin defects and (K) corresponding analysis. \* $p < 0.05$ , \*\* $p < 0.01$ , \*\*\* $p < 0.001$  by ANOVA for data in (I) and (K). Different letters indicate significant differences.

process for maintaining cell homeostasis and organelle renewal, is a pivotal factor in inducing macrophages to reprogram from a pro-inflammatory phenotype to a pro-healing and pro-resolving phenotype during wound healing, as alternatively activated pathways play little role in macrophage phenotype reprogramming *in vivo* [59,60]. As shown in Fig. 6C–E, the results of top 10 in KEGG show that the significantly upregulated signal pathways items associated with A300, relative to control and A1000 groups, include primarily *lysosome* and *phagosome*. The heat maps derived from *lysosome* and *phagocytosis* items (Fig. 6F and G) also show genes related to phenotype transformation of macrophages. Additionally, the macrophage-related genes that displayed significant changes have been shown as heat maps. We observed that the expression of reparative macrophages associated with A300 is similar to that of A600 yet much stronger than that of the control group and A1000, according to the heat maps (Fig. 6H). It has been reported that inflammatory macrophages could inhibit keratinocyte migration, which is harmful to wound healing [61,62]. The RNA expression analysis of Cd68, interleukin 10 (IL10), and transforming growth factor  $\beta$  (TGF $\beta$ ) (Fig. 6I) also show that the A300-treated group is significantly upregulated compared to other groups, corroborating prior evidence that A300 aligned membranes indeed promote immune related processes towards a pro-healing direction. As shown in Fig. S8, the gene changes of reparative macrophages are more significant than that of

neutrophils and T cells, indicating that reparative macrophages play a more important role than other immune cells. Based on Fig. S9, the expression trend of IL-10 is similar to that of Cd206, indicating that more reparative macrophages appear in the A300-treated group. Moreover, the autophagy marker microtubule-associated protein 1A/1B-light chain 3 (LC3B, IHC staining) (Fig. 6J–K) corroborates the above results shown in the gene heat maps. Taken altogether, the results indicate that A300 aligned membranes facilitate tissue regenerative immune reactions.

## 2.6. MMP12 secreted by macrophages on A300 membranes promotes keratinocyte migration

We further explored the effect of aligned membranes on macrophages. The workflow for verifying the function of macrophages and MMP12 *in vitro* is summarized in Fig. 7A. The results of IF staining show that the adhesion and extension of macrophages (area/number) on A300 membranes are better than on other diameter membranes (Fig. 7B and C), suggesting that A300 manipulates the behavior of macrophages. Through the cell scratch test, it was observed that, the macrophage-conditioned medium of A300 promotes the migration of keratinocytes (Fig. 7D and E). Furthermore, the expression of MMP12 and reparative marker of macrophages is more significant in the A300-treated group



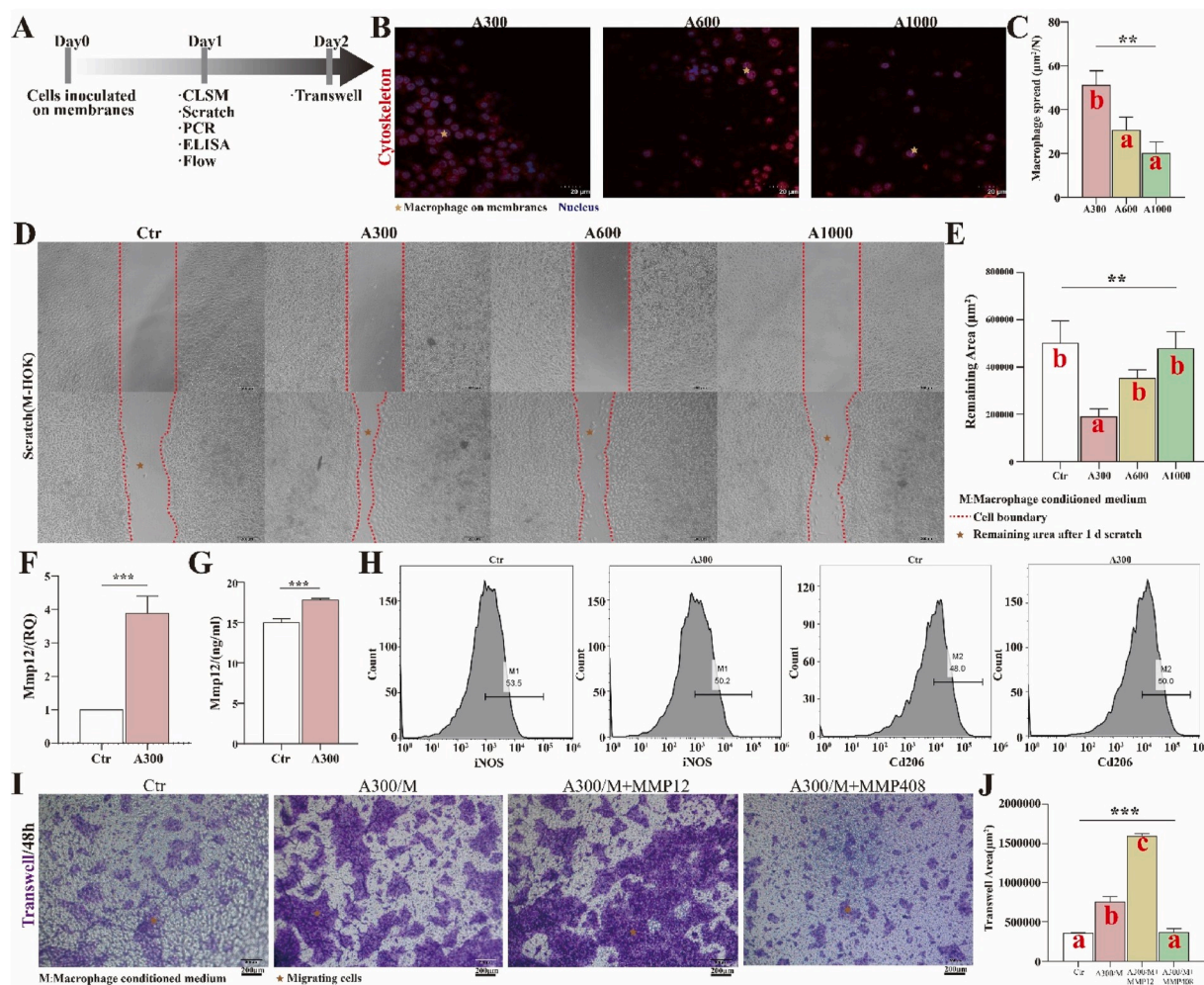


**Fig. 7.** (A) Workflow for verifying the function of macrophages and MMP12 *in vitro*; (B) CLSM images of macrophages (Thp1) on different diameter electrospinning membranes and (C) corresponding analysis; (D) The migration of HOK stimulated by the conditioned medium derived from macrophages inoculated on various membranes and (E) corresponding analysis; (F) RNA expression of MMP12; (G) ELISA result of MMP12; (H) Flow cytometry results of macrophages; (I) Transwell assays and (J) corresponding analysis. \* $p < 0.05$ , \*\* $p < 0.01$ , \*\*\* $p < 0.001$  by ANOVA for data in (C), (E), (F), (G), and (J). Different letters indicate significant differences.

(Fig. 7F–H). More importantly, the recombinant protein MMP12 could enhance the promoting migration effect of macrophage-conditioned medium from the A300-treated group, while the MMP12 inhibitor could largely inhibit this effect (Fig. 7I and J). All these results indicate that MMP12, which is secreted by macrophages, promotes keratinocyte migration.

### 3. Discussion

In this study, we fabricated aligned membranes with three fiber diameters (A300, A600, and A1000). The A300 membranes lead to faster wound healing and reduced FBR compared to other groups. Specifically, A300 aligned membranes enhance vascularization (increased area of new blood vessels), which is the cornerstone of wound healing. It is widely acknowledged that the newly formed blood vessels could provide the necessary nutrients necessary for accelerating wound healing [63]. The A300 membranes bring about preferable epithelialization (improved maturity and integrity) with regeneration of immature HFs, which is key to wound healing. HF regeneration is one of the important indexes of functional skin healing [5]. It has been reported that HF stem cells could accelerate wound healing as well as tensile strength [64]. Additionally, the A300 membranes exhibit immunomodulatory properties (Fig. 3G–J). Based on this evidence, we generated bulk RNA from

wounded rat skin (7 d) to investigate the microenvironment around the membranes. Compared to the control group and A1000 membranes, the A300 and A600 membranes significantly increase the expression of genes related to reparative macrophages (Fig. 6). Considering that A300 has the best repair effect, we focused our attention on this fiber diameter. MMP12, predominantly expressed by macrophages [58], is significantly differentially expressed both in *positive regulation of immune response* and *innate immune response* GO items (Fig. 5). It has been reported that TIMP (tissue inhibitor of metalloproteinase)-1 significantly reduces the migration ability of keratinocytes [61]. Another study has revealed that MMP12 actively regulates the migration of cells and protects against corneal fibrosis in the process of corneal wound healing [56,57]. We speculated that MMP12 has a similar role in skin wound healing. Through the use of a recombinant protein and an inhibitor of MMP12, we corroborated that MMP12 indeed facilitates the migration and spread of epidermal cells *in vitro* (Figs. 5 and 7). The workflow for verifying the function of MMP12 in mice is summarized in Fig. S10, and it further shows that proper concentrations of MMP12 could accelerate epithelialization and achieve complete wound healing. Furthermore, small diameter aligned membranes with another composition, such as gelatin, also accelerate epithelialization and resulting wound healing compared to large diameter membranes (Fig. S11). We conclude that A300 aligned membranes could facilitate tissue regenerative immune

reactions, subsequently promoting epidermal cell migration and final wound healing.

#### 4. Conclusions

In the present studies, aligned membranes with different fiber diameters were successfully prepared via electrospinning, a technique that is capable of creating membranes that imitate the component and spatial structure of the skin ECM. Compared to other membranes, the A300 group enhances mechanical strength and hydrophilicity, regulates the degradation rate of the membranes as desired, and promotes cell proliferation and spreading. In particular, A300 aligned membranes significantly facilitate skin wound healing (vascularization and epithelization) with HFs. Additionally, transcriptome analysis reveals the underlying molecular mechanism that A300 aligned membranes could facilitate tissue regenerative immune reactions and promote epidermal cell migration via secretion of MMP12. Taken together, we consider that wound healing requires the active participation of the immune process, and that the A300 aligned membrane is a preferable design. Therefore, A300 aligned membranes are a potential candidate for guided skin regeneration applications, particularly for re-epithelization. However, more diameter groups and regenerative immune processes still need to be investigated.

#### 5. Experimental section

##### 5.1. Materials

Poly (lactide-co-glycolide) (PLGA, LA/GA = 75:25, MW = 105 kDa, dispersity of 1.897) was purchased from Jinan Daigang Biomaterial Co., Ltd. (Shandong, China). Fish collagen (FC) from fish scale and skin was procured from Sangon Biotech Co., Ltd. (Shanghai, China). 1,1,1,3,3,3-Hexafluoro-2-propanol (HFIP), N-hydroxysuccinimide (NHS), and 1-ethyl-3-(3-dimethylaminopropyl) carbodiimide hydrochloride (EDC) were offered by Aladdin Co., Ltd. (Shanghai, China).

##### 5.2. Preparation of aligned membranes with different diameters via electrospinning

To fabricate the aligned FC-reinforced PLGA electrospinning membrane (FC/PLGA) with different fiber diameters, PLGA and FC were dissolved in HFIP with stirring at 25 °C. The solution was stirred vigorously until complete dissolution of PLGA and FC. Subsequently, the prepared electrospinning solutions were employed to fabricate fibrous aligned membranes with different fiber diameters via electrospinning in the following manner. The electrospinning solutions were loaded into a plastic syringe fitted with a flat-tipped 21 G stainless steel needle. A high voltage and a distance were applied between the needle and the roller collector (2800 rpm), which was covered with a piece of aluminum foil. The solution was fed at a constant speed, regulated by a precision syringe pump. The prepared membranes were dried in a vacuum oven at 25 °C until the solvent was completely volatilized, which was confirmed by the X-ray diffraction (XRD) and Fourier transform infrared spectroscopy (FTIR) spectra (Figs. S2E and S2F).

##### 5.3. Characterization

An SEM (JEOL, JSM-6510LV, Japan) was employed to observe the morphology of the aligned membranes with different diameters. In addition, Image-Pro Plus was used to quantitatively measure diameter, distribution, and alignment (orientation < 10°) [65] from the SEM images obtained for 200 randomly selected fibers. To estimate the mechanical performance of these membranes, the samples were attached to an electronic universal testing machine (SHIMADZU, AG-IC 50 KN, Japan) with a 50-N load cell. Prior to testing, samples with thicknesses of 0.1–0.2 mm were cut into a dumbbell shape with a gauge length of 75

mm and width of 4 mm. The tensile properties of membranes were determined under a constant upper clamp speed of 5 mm/min at room temperature, in accordance with the criteria of “Plastics-Determination of tensile properties of films” (GB/T 1040.3–2006, corresponding with ISO 1184–1983). The elastic modulus was calculated from the slope of the linear region ( $\epsilon = 1\text{--}3\%$ ) of the stress-strain curve. Atomic force microscopy (AFM; JEOL, JSM-6510LV, Japan) was employed to observe the roughness of the aligned membranes with different diameters. The surface wetting behavior of the membranes was characterized by measuring the water contact angles using a contact angle measuring instrument (Chengde Dingsheng, JY-82B, China) and a hydrophilicity test. Five samples were tested for each membrane group to obtain an average value.

##### 5.4. In vitro swelling and degradability study

The aligned membranes with different diameters were immersed in a solution of 50 mM EDC/NHS and 10 mM of ethanol for 24 h at 4 °C. The membranes were washed three times with ethanol and then dried in a vacuum oven for 24 h. The dried fibrous membranes were cut into 10 mm × 10 mm squares and weighed accurately. The membrane samples were put into 5 mL plastic tubes containing 4 mL phosphate buffered saline (PBS, pH = 7.4) and were put in a shaking incubator at 100 rpm and 37 °C. The incubating media were changed every week. At each predetermined time point, the samples were dried to a constant weight in a vacuum oven. The swelling and weight loss rate were calculated according to the following formula:

$$\text{Weight remaining (\%)} = m / m_0 \times 100\%$$

Where  $m_0$  is the mass of the membrane before incubation and  $m$  is the mass of the membrane after incubation for a set time.

##### 5.5. In vitro cell culture experiments

###### 5.5.1. Cell culture

The fibroblasts (L929), human oral keratinocytes (HOK), and Thp1 were obtained from West China School of Stomatology, Sichuan University. L929, HOK, and Thp1 were cultured in modified RPMI medium (1640; Gibco, USA) supplemented with 10% fetal bovine serum (FBS, Gibco, USA) and a 1% mixture of penicillin/streptomycin (MP Bio-medicals, USA). The culture medium was replaced every other day in the L929, HOK, and Thp1 culture cycle. On reaching a confluence of 80%–90%, Thp1 was induced into macrophages with propylene glycol methyl ether acetate (PMA, 100 ng/mL). Membranes were preprocessed by immersing in a 75% ethanol solution for 30 min. Subsequently, all the prepared membranes were sterilized by  $\gamma$ -irradiation for cell experiments.

###### 5.5.2. Cell viability

L929, HOK, and Thp1 ( $1 \times 10^4$  cells/well) were seeded and incubated separately at 37 °C with 5% CO<sub>2</sub> atmosphere. One day after culturing on membranes, the macrophage supernatant was collected for follow-up experiments. At the given time points (1 d, 3 d, 5 d, 7 d), the proliferation of L929 and HOK on these membranes was assessed by cell counting kit-8 (CCK-8, DOJINDO, Japan) assay. Membrane materials were not used in the control group. The optical density (OD) value was read by a 1420 Multilabel Counter (PerkinElmer, USA) at 450 nm. The dead portion of HOK was stained with propidium iodide (PI), according to the product instructions (DOJINDO, Japan). Fluorescence images were visualized with an inverted fluorescence microscope (Leica, Germany). SEM (JEOL, JSM-6510LV, Japan) was employed to observe the morphology of cells on the aligned membranes. Random membrane materials were used in the control group. The macrophages were stained with phalloidin, according to product instructions (Solarbio, USA). Fluorescence images were visualized with a confocal laser scanning

microscope (CLSM, Leica, Germany).

### 5.5.3. Cell migration

HOK cells ( $1 \times 10^5$  cells/well) were seeded in the chamber of *trans*-well and 24-pore plates at 37 °C with 5% CO<sub>2</sub> atmosphere. Different stimuli, such as MMP12 (1 μL, 20 ng/mL, Biolegend, USA), MMP408 (1 μL, 20 ng/mL, Invivogen, USA) and macrophage supernatants, were added. At the given time point (2 d), HOK cells in the plates were fixed (30 min). HOK cells in the chambers of the *trans*-well plates were stained with crystal violet (0.1% w/v, 30 min), washed with PBS, and visualized with an inverted microscope (Leica, Germany). The HOK cells in the 24-pore plate were stained with phalloidin, according to the product instructions (Solarbio, China). Fluorescence images were visualized with a confocal laser scanning microscope (CLSM, Leica, Germany).

### 5.5.4. Flow cytometry

Macrophages (transformed from Thp1) were collected into EP tubes after 24 h, fixed with 4% paraformaldehyde for 15 min, centrifuged and washed with PBS a total of 3 times, and blocked with 3% BSA. Macrophages were mixed with the corresponding direct labeling antibody (iNOS, ab115819, 1:200; Cd206, ab195192, 1:200) prepared in a 1% BSA solution, incubated at 4 °C for 1 h, and washed 3 times with PBS. The corresponding indicators were detected on a flow cytometer (Thermo Fisher, USA).

### 5.6. Animal experiments

Sprague–Dawley (SD) rats, aged 8 weeks and with an average weight of 220 ± 20 g (C57BL/6 mice aged 8 weeks with an average weight of 20 g used in the supplementary section), were obtained from the Experimental Animal Center of Sichuan University. All studies were approved by the Institution Review Board of West China Hospital of Stomatology (No. WCHSIRB-D-2017-033-R1). The experimental rats could access food and water at will. The health status of the rats was checked every day during the experimental period. After conventional fasting for 12 h, the rats were intraperitoneally anaesthetized in accordance with the instructions of the Animal House. After skin preparation for surgery, a circular defect with a 6 mm diameter was created on the right and left skin of the dorsum. After transplanting different diameter aligned electrospinning membranes, the skin wounds were covered with 3 M™ Tegaderm™ and fixed on the latex ring with 3.0 silk suture. The experimental rats received routine postoperative nursing [66]. The experimental rats were randomly divided into four groups: skin wounds transplanted with saline (Ctr), A300 aligned membranes, A600 aligned membranes, and A1000 aligned membranes. The rats were executed by dislocation after anesthesia 5, 7, and 14 days after surgery, and tissue samples for general analysis were harvested. All tissue sections that were obtained from the rat skin wounds for routine histological examination were stained with MST Staining. The thickness of fibrous capsule was determined manually under a microscope, using 5 randomly picked fields (at 100 × magnification). Immunohistochemistry (IHC) was performed for CD31 (ab182981, Abcam, 1:2000) to evaluate vascularization, and for LC3B (Sigma-Aldrich, L7543, 1:200, USA) to evaluate autophagy. Double staining immunofluorescence (IF) was performed for cytokeratin 5 (K5, ab52635, Abcam, 1:200) and cytokeratin 10 (K10, ab76318, Abcam, 1:150) to evaluate keratinization. IHC results were further verified by qRT-PCR, and the data were presented as the relative quantification (RQ,  $2^{-\Delta\Delta C_t}$ ) compared to control groups (related primers are shown in Table S2).

### 5.7. Bulk RNA sequencing

Three replicates of rat skin wounds in each group were detected for the assay of Bulk RNA sequencing (NEBNext® Ultra™ RNA Library Prep Kit for Illumina®), and the results were analyzed for GO and KEGG for screening the related targets. These results were further verified by

fluorescence quantitative PCR (related primers are shown in Table S2) and ELISA (MEIMIAN, China).

### 5.8. Statistical analysis

At least three independent assays were conducted to obtain repeatable data if not distinctively explained, and the data was dealt with Case Viewer, Origin 2019 or Graphpad Prism 8.0 software. Statistical analyses were performed by Student's t-test and the Tukey post-hoc test by analysis of variance under the condition of normal distribution. The numerical data are presented as mean ± standard error of the mean. A value of  $p < 0.05$  was considered statistically significant (\* $p < 0.05$ , \*\* $p < 0.01$ , \*\*\* $p < 0.001$ ).

### CRedit authorship contribution statement

**Chenbing Wang:** Formal analysis, Investigation, Validation, Writing – original draft, Resources. **Chenyu Chu:** Project administration, Methodology, Writing – review & editing. **Xiwen Zhao:** Formal analysis, Data curation, Investigation. **Yang Yang:** Software, Data curation. **Chen Hu:** Data curation. **Li Liu:** Resources. **Jidong Li:** Resources. **Yili Qu:** Funding acquisition. **Yi Man:** Project administration, Funding acquisition, Supervision.

### Declaration of competing interest

The authors state no conflict of interest.

### Acknowledgments

This work was supported by Key R & D Projects of Sichuan Science and Technology Plan (2021YFS0030), Interdisciplinary Innovation Project, West China Hospital of Stomatology Sichuan University (RD-03-202006), and Research and Develop Program, West China Hospital of Stomatology Sichuan University (No. LCYJ2019-19). We would like to thank the Novogene company for Bulk RNA sequencing work, thank the National Clinical Research Center for Oral Diseases & State Key Laboratory of Oral Diseases for atomic force microscopy work, and thank the Analytical & Testing Center of Sichuan University for tensile strength image work.

### Appendix A. Supplementary data

Supplementary data to this article can be found online at <https://doi.org/10.1016/j.bioactmat.2021.09.022>.

### References

- [1] A. Amirsadeghi, A. Jafari, L.J. Eggermont, et al., Vascularization strategies for skin tissue engineering[J], *Biomater Sci* 8 (15) (2020) 4073–4094.
- [2] Y. Zhao, Z. Li, S. Song, et al., Skin-inspired antibacterial conductive hydrogels for epidermal sensors and diabetic foot wound dressings[J], *Adv. Funct. Mater.* 29 (2019).
- [3] C.K. Sen, G.M. Gordillo, S. Roy, et al., Human skin wounds: a major and snowballing threat to public health and the economy[J], *Wound Repair Regen.* 17 (6) (2009) 763–771.
- [4] S.O. Blacklow, J. Li, B.R. Freedman, et al., Bioinspired mechanically active adhesive dressings to accelerate wound closure[J], *Sci Adv* 5 (7) (2019), eaaw3963.
- [5] Mascharak S, Desjardins-Park H E, Davitt M F, et al. Preventing Engrailed-1 activation in fibroblasts yields wound regeneration without scarring[J]. *Science*, 2021, 372(6540).
- [6] H. Savoji, B. Godau, M.S. Hassani, et al., Skin tissue substitutes and biomaterial risk assessment and testing[J], *Front Bioeng Biotechnol* 6 (2018) 86.
- [7] P.H. Wang, B.S. Huang, H.C. Horng, et al., Wound healing[J], *J. Chin. Med. Assoc.* 81 (2) (2018) 94–101.
- [8] L. Cui, J. Liang, H. Liu, et al., Nanomaterials for angiogenesis in skin tissue engineering[J], *Tissue Eng. B Rev.* 26 (3) (2020) 203–216.
- [9] J. Larouche, S. Sheoran, K. Maruyama, et al., Immune regulation of skin wound healing: mechanisms and novel therapeutic targets[J], *Adv. Wound Care* 7 (7) (2018) 209–231.



- [10] A.D. Juncos Bombin, N.J. Dunne, H.O. McCarthy, Electrospinning of natural polymers for the production of nanofibres for wound healing applications[J], *Mater Sci Eng C Mater Biol Appl* 114 (2020) 110994.
- [11] A.P. Kishan, E.M. Cosgriff-Hernandez, Recent advancements in electrospinning design for tissue engineering applications: a review[J], *J. Biomed. Mater. Res.* 105 (10) (2017) 2892–2905.
- [12] P. Friedl, K. Wolf, Plasticity of cell migration: a multiscale tuning model[J], *J. Cell Biol.* 188 (1) (2010) 11–19.
- [13] D.T. Scadden, Nice neighborhood: emerging concepts of the stem cell niche[J], *Cell* 157 (1) (2014) 41–50.
- [14] S.P. Miguel, D.R. Figueira, D. Simões, et al., Electrospun polymeric nanofibres as wound dressings: a review[J], *Colloids Surf. B Biointerfaces* 169 (2018) 60–71.
- [15] M.O. Dellacherie, B.R. Seo, D.J. Mooney, Macroscale biomaterials strategies for local immunomodulation[J], *Nature Reviews Materials* 4 (6) (2019) 379–397.
- [16] K. Sadtler, A. Singh, M.T. Wolf, et al., Design, clinical translation and immunological response of biomaterials in regenerative medicine[J], *Nature Reviews Materials* 1 (7) (2016) 16040.
- [17] Y. Wang, H. Shi, J. Qiao, et al., Electrospun tubular scaffold with circumferentially aligned nanofibers for regulating smooth muscle cell growth[J], *ACS Appl. Mater. Interfaces* 6 (4) (2014) 2958–2962.
- [18] S. Nour, R. Imani, G.R. Chaudhry, et al., Skin wound healing assisted by angiogenic targeted tissue engineering: a comprehensive review of bioengineered approaches [J], *J. Biomed. Mater. Res.* (2020).
- [19] A.D. Doyle, N. Carvajal, A. Jin, et al., Local 3D matrix microenvironment regulates cell migration through spatiotemporal dynamics of contractility-dependent adhesions[J], *Nat. Commun.* 6 (2015) 8720.
- [20] Y. Liu, A. Franco, L. Huang, et al., Control of cell migration in two and three dimensions using substrate morphology[J], *Exp. Cell Res.* 315 (15) (2009) 2544–2557.
- [21] J. Xie, M.R. Macewan, W.Z. Ray, et al., Radially aligned, electrospun nanofibers as dural substitutes for wound closure and tissue regeneration applications[J], *ACS Nano* 4 (9) (2010) 5027–5036.
- [22] P.W. Alford, A.P. Nesmith, J.N. Seywerd, et al., Vascular smooth muscle contractility depends on cell shape[J], *Integr Biol (Camb)* 3 (11) (2011) 1063–1070.
- [23] C. Hu, C. Chu, L. Liu, et al., Dissecting the microenvironment around biosynthetic scaffolds in murine skin wound healing[J], *Science Advances* 7 (22) (2021), eabf0787.
- [24] M. Abrigo, S.L. McArthur, P. Kingshott, Electrospun nanofibers as dressings for chronic wound care: advances, challenges, and future prospects[J], *Macromol. Biosci.* 14 (6) (2014) 772–792.
- [25] R. Mcbeath, D.M. Pirone, C.M. Nelson, et al., Cell shape, cytoskeletal tension, and RhoA regulate stem cell lineage commitment[J], *Dev. Cell* 6 (4) (2004) 483–495.
- [26] J. Xie, H. Shen, G. Yuan, et al., The effects of alignment and diameter of electrospun fibers on the cellular behaviors and osteogenesis of BMSCs[J], *Mater Sci Eng C Mater Biol Appl* 120 (2021) 111787.
- [27] A. Jafari, A. Amirsadeghi, S. Hassanajili, et al., Bioactive antibacterial bilayer PCL/gelatin nanofibrous scaffold promotes full-thickness wound healing[J], *Int. J. Pharm.* 583 (2020) 119413.
- [28] S.G. Kumbar, S.P. Nukavarapu, R. James, et al., Electrospun poly(lactic acid-co-glycolic acid) scaffolds for skin tissue engineering[J], *Biomaterials* 29 (30) (2008) 4100–4107.
- [29] Y. Liu, Y. Ji, K. Ghosh, et al., Effects of fiber orientation and diameter on the behavior of human dermal fibroblasts on electrospun PMMA scaffolds[J], *J. Biomed. Mater. Res.* 90 (4) (2009) 1092–1106.
- [30] T. Hodgkinson, X.F. Yuan, A. Bayat, Electrospun silk fibroin fiber diameter influences in vitro dermal fibroblast behavior and promotes healing of ex vivo wound models[J], *J. Tissue Eng.* 5 (2014), 2041731414551661.
- [31] J. Wang, L. Wang, M. Yang, et al., Untangling the effects of peptide sequences and nanotopographies in a biomimetic niche for directed differentiation of iPSCs by assemblies of genetically engineered viral nanofibers[J], *Nano Lett.* 14 (12) (2014) 6850–6856.
- [32] A. Shams, N. Eslahi, M. Movahedin, et al., Future of spermatogonial stem cell culture: application of nanofiber scaffolds[J], *Curr. Stem Cell Res. Ther.* 12 (7) (2017) 544–553.
- [33] M.C. Amores De Sousa, C. a V. Rodrigues, I. a F. Ferreira, et al., Functionalization of electrospun nanofibers and fiber alignment enhance neural stem cell proliferation and neuronal differentiation[J], *Front Bioeng Biotechnol* 8 (2020) 580135.
- [34] E. Saino, M.L. Focarete, C. Gualandi, et al., Effect of electrospun fiber diameter and alignment on macrophage activation and secretion of proinflammatory cytokines and chemokines[J], *Biomacromolecules* 12 (5) (2011) 1900–1911.
- [35] X. Zheng, L. Xin, Y. Luo, et al., Near-infrared-triggered dynamic surface topography for sequential modulation of macrophage phenotypes[J], *ACS Appl. Mater. Interfaces* 11 (46) (2019) 43689–43697.
- [36] H. Chen, Y. Qian, Y. Xia, et al., Enhanced osteogenesis of ADSCs by the synergistic effect of aligned fibers containing collagen II[J], *ACS Appl. Mater. Interfaces* 8 (43) (2016) 29289–29297.
- [37] S. Jin, F. Sun, Q. Zou, et al., Fish collagen and hydroxyapatite reinforced poly(lactide-co-glycolide) fibrous membrane for guided bone regeneration[J], *Biomacromolecules* 20 (5) (2019) 2058–2067.
- [38] R.A. Gittens, R. Olivares-Navarrete, T. Mclachlan, et al., Differential responses of osteoblast lineage cells to nanotopographically-modified, microroughened titanium-aluminum-vanadium alloy surfaces[J], *Biomaterials* 33 (35) (2012) 8986–8994.
- [39] Z. Chen, A. Bachhuka, S. Han, et al., Tuning chemistry and topography of nanoengineered surfaces to manipulate immune response for bone regeneration applications[J], *ACS Nano* 11 (5) (2017) 4494–4506.
- [40] E.J. Mulholland, Electrospun biomaterials in the treatment and prevention of scars in skin wound healing[J], *Front Bioeng Biotechnol* 8 (2020) 481.
- [41] U. Stachewicz, R. Bailey, W. Wang, et al., Size dependent mechanical properties of electrospun polymer fibers from a composite structure[J], *Polymer* 53 (2012) 5132.
- [42] E.P. Tan, S.Y. Ng, C.T. Lim, Tensile testing of a single ultrafine polymeric fiber[J], *Biomaterials* 26 (13) (2005) 1453–1456.
- [43] S. Giljean, M. Bigerelle, K. Anselme, Roughness statistical influence on cell adhesion using profilometry and multiscale analysis[J], *Scanning* 36 (1) (2014) 2–10.
- [44] S.P. Miguel, R.S. Sequeira, A.F. Moreira, et al., An overview of the electrospun membranes loaded with bioactive molecules for improving the wound healing process[J], *Eur. J. Pharm. Biopharm.* 139 (2019) 1–22.
- [45] G. Huang, F. Li, X. Zhao, et al., Functional and biomimetic materials for engineering of the three-dimensional cell microenvironment[J], *Chem. Rev.* 117 (20) (2017) 12764–12850.
- [46] S. Zhong, W.E. Teo, X. Zhu, et al., An aligned nanofibrous collagen scaffold by electrospinning and its effects on in vitro fibroblast culture[J], *J. Biomed. Mater. Res.* 79 (3) (2006) 456–463.
- [47] M.D. Chomachayi, A. Solouk, H. Mirzadeh, Electrospun silk-based nanofibrous scaffolds: fiber diameter and oxygen transfer[J], *Prog Biomater* 5 (2016) 71–80.
- [48] F. Tian, H. Hosseinkhani, M. Hosseinkhani, et al., Quantitative analysis of cell adhesion on aligned micro- and nanofibers[J], *J. Biomed. Mater. Res.* 84 (2) (2008) 291–299.
- [49] S. Lavenus, P. Pilet, J. Guicheux, et al., Behaviour of mesenchymal stem cells, fibroblasts and osteoblasts on smooth surfaces[J], *Acta Biomater.* 7 (4) (2011) 1525–1534.
- [50] B.M. Baker, B. Trappmann, W.Y. Wang, et al., Cell-mediated fibril recruitment drives extracellular matrix mechanosensing in engineered fibrillar microenvironments[J], *Nat. Mater.* 14 (12) (2015) 1262–1268.
- [51] S. Franz, S. Rammelt, D. Scharnweber, et al., Immune responses to implants - a review of the implications for the design of immunomodulatory biomaterials[J], *Biomaterials* 32 (28) (2011) 6692–6709.
- [52] J.M. Anderson, A. Rodriguez, D.T. Chang, Foreign body reaction to biomaterials [J], *Semin. Immunol.* 20 (2) (2008) 86–100.
- [53] C. Chu, L. Liu, S. Rung, et al., Modulation of foreign body reaction and macrophage phenotypes concerning microenvironment[J], *J. Biomed. Mater. Res.* (2019).
- [54] J.D. Bryers, C.M. Giachelli, B.D. Ratner, Engineering biomaterials to integrate and heal: the biocompatibility paradigm shifts[J], *Biotechnol. Bioeng.* 109 (8) (2012) 1898–1911.
- [55] F. Chen, Q. Zhang, P. Wu, et al., Green fabrication of seedbed-like *Flammulina velutipes* polysaccharides-derived scaffolds accelerating full-thickness skin wound healing accompanied by hair follicle regeneration[J], *Int. J. Biol. Macromol.* 167 (2021) 117–129.
- [56] M. Wolf, I. Malteva, S.M. Clay, et al., Effects of MMP12 on cell motility and inflammation during corneal epithelial repair[J], *Exp. Eye Res.* 160 (2017) 11–20.
- [57] M.F. Chan, J. Li, A. Bertrand, et al., Protective effects of matrix metalloproteinase-12 following corneal injury[J], *J. Cell Sci.* 126 (Pt 17) (2013) 3948–3960.
- [58] S.D. Shapiro, D.K. Kobayashi, T.J. Ley, Cloning and characterization of a unique elastolytic metalloproteinase produced by human alveolar macrophages[J], *J. Biol. Chem.* 268 (32) (1993) 23824–23829.
- [59] J.M. Daley, S.K. Brancato, A.A. Thomay, et al., The phenotype of murine wound macrophages[J], *J. Leukoc. Biol.* 87 (1) (2010) 59–67.
- [60] M.R. Elliott, K.M. Koster, P.S. Murphy, Efferocytosis signaling in the regulation of macrophage inflammatory responses[J], *J. Immunol.* 198 (4) (2017) 1387–1394.
- [61] S.M. Huang, C.S. Wu, M.H. Chiu, et al., High glucose environment induces M1 macrophage polarization that impairs keratinocyte migration via TNF- $\alpha$ : an important mechanism to delay the diabetic wound healing[J], *J. Dermatol. Sci.* 96 (3) (2019) 159–167.
- [62] M.L. Usui, J.N. Mansbridge, W.G. Carter, et al., Keratinocyte migration, proliferation, and differentiation in chronic ulcers from patients with diabetes and normal wounds[J], *J. Histochem. Cytochem.* 56 (7) (2008) 687–696.
- [63] T.G. Sahana, P.D. Rekha, Biopolymers: applications in wound healing and skin tissue engineering[J], *Mol. Biol. Rep.* 45 (6) (2018) 2857–2867.
- [64] A. Babakhani, M. Nobakht, H. Pazoki Torodi, et al., Effects of hair follicle stem cells on partial-thickness burn wound healing and tensile strength[J], *Iran. Biomed. J.* 24 (2) (2020) 99–109.
- [65] S.-D. Liu, D.-S. Li, Y. Yang, et al., Fabrication, mechanical properties and failure mechanism of random and aligned nanofiber membrane with different parameters [J], *Nanotechnol. Rev.* 8 (2019) 218–226.
- [66] M.R. Da Cunha, F.A. Menezes, G.R. Dos Santos, et al., Hydroxyapatite and a new fibrin sealant derived from snake venom as scaffold to treatment of cranial defects in rats[J], *Materials Research-Ibero-American Journal of Materials* 18 (1) (2015) 196–203.